

Research Article

Resonance Mechanism of Nonlinear Vibrational Multistable Energy Harvesters under Narrow-Band Stochastic Parametric Excitations

Dongmei Huang ^{1,2}, Shengxi Zhou ¹, and Zhichun Yang¹

¹School of Aeronautics, Northwestern Polytechnical University, Xi'an 710072, China

²School of Mathematics and Statistics, Xidian University, Xi'an, Shaanxi 710071, China

Correspondence should be addressed to Shengxi Zhou; zhoushengxi@nwpu.edu.cn

Received 4 February 2019; Revised 26 October 2019; Accepted 6 November 2019; Published 14 December 2019

Academic Editor: Bernhard C. Geiger

Copyright © 2019 Dongmei Huang et al. This is an open access article distributed under the Creative Commons Attribution License, which permits unrestricted use, distribution, and reproduction in any medium, provided the original work is properly cited.

To improve energy harvesting performance, this paper investigates the resonance mechanism of nonlinear vibrational multistable energy harvesters under narrow-band stochastic parametric excitations. Based on the method of multiple scales, the largest Lyapunov exponent which determines the stability of the trivial steady-state solutions is derived. The first kind modified Bessel function is utilized to derive the solutions of the responses of multistable energy harvesters. Then, the first-order and second-order nontrivial steady-state moments of multistable energy harvesters are considered. To explore the stochastic bifurcation phenomenon between the nontrivial and trivial steady-state solutions, the Fokker–Planck–Kolmogorov equation corresponding to the two-dimensional Itô stochastic differential equations is solved by using the finite difference method. In addition, the mechanism of the stochastic bifurcation of multistable energy harvesters is analyzed for revealing their unique dynamic response characteristics.

1. Introduction

Vibration energy harvesting is expected to replace some small traditional chemical batteries and permanently supply power for the low-powered wireless sensors and actuators and also can promote structural health monitoring [1–5]. Recently, vibrational nonlinear energy harvesters have been receiving more and more attention because they have the better energy harvesting performance than traditional linear energy harvesters under time-varying ambient environmental excitations [4–9]. By far, different kinds of high-performance nonlinear energy harvesters have been designed based on geometric nonlinearity, additional nonlinear magnetic force, residual thermal stress, or active/passive control strategies [9–12].

In past several years, the novel methods to broaden the bandwidth are achieved by introducing nonlinearity and multioscillator structures, and the nonlinear behaviors may

extend the operating bandwidth of the energy harvester, allowing for efficient energy harvesting under random vibrations. Nonlinear energy harvesters with monostable, bistable, tristable, and even quadstable characteristics have been extensively studied to improve the harvesting performance in natural. Cottone et al. [12] designed a bistable energy harvester (BEH) based on additional nonlinear magnetic force and a cantilever beam structure, and they experimentally verified its advantage for harvesting energy from random vibrations. Later on, Litak et al. [13, 14] deeply investigated and verified the energy harvesting improvement of the BEH under random base excitations. Chen and Jiang [15] presented the internal resonance mechanism to enhance vibration energy harvesting. Wang et al. [16] experimentally tested a BEH to harvest energy from human motions, and a better energy harvesting performance over the linear monostable harvester was archived. Then, Zhou et al. [17] designed a tristable energy harvester (TEH) to improve the

broadband energy harvesting performance from low-level ambient vibrations. The TEH physically has three potential energy wells, which may have lower potential barriers than the BEH [18]. The advantages of the TEH in broadband vibration energy harvesting over the BEH under low-level harmonic and random base excitations were experimentally and numerically verified [17, 19–21]. For example, Xu et al. [22] revealed the stochastic resonance mechanism of the TEH. Tékam et al. [23] studied the influence of the fractional-order viscoelastic material of a TEH on its energy harvesting performance. The influence mechanism of the system parameters of the TEH on the dynamic responses and the energy harvesting performance was completely provided in [24–26].

In recent years, based on the magnetic coupled energy harvesting structures, Zhou et al. [27, 28] developed multistable energy harvesters with four or five stable equilibrium positions, and a better energy harvesting performance over the BEH was verified. For the real application, Younesian and Alam [29] designed broadband multistable wave energy harvesters based on the multistable mechanism, and the designed harvesters were verified to have high-efficiency energy harvesting performance. Gao et al. [30] presented a multistable energy harvester based on the magnetic levitation oscillation, and it has the quadstable configuration. In the railway test, the RMS power output is 440.98 mW, which is large enough to power some small wireless sensor nodes. Under harmonic base excitations, the theoretical solutions of nonlinear vibrational multistable energy harvesters were provided by Huang et al. [31]. These research studies verify the high-efficiency energy harvesting performance of multistable energy harvesters in experiments and real environmental tests.

In practice, the operation of the piezoelectric system is highly susceptible to the various random factors from internal and external environment fluctuation [32–39], for example, the devices which are manufactured by the piezoelectric ceramic widely used in meteorological observation and household appliances; the normal operation of these devices are often influenced by the atmospheric turbulence, voltage fluctuation, and even other random disturbance. Thus, the nonlinear energy harvesters, especially in stochastic vibratory environments, have become an unavoidable topic [34–40]. Xu et al. [34] developed the stochastic averaging technique for the energy harvester under Gaussian white noise excitation to evaluate the mean-square electric voltage and mean output power. They also considered the responses of bistable energy harvester under additive and multiplicative white noises [35]. Jiang and Chen [36, 37] analyzed the response of nonlinear energy harvesters subject to external Gaussian white noise and parametric excitations. He and Daqaq [38] illustrated the optimal potential shape on the mean output power through the statistical linearization techniques. Recently, Liu et al. [39] proposed a new quasi-conservative stochastic averaging method to discuss the probabilistic response of the nonlinear energy harvesting system subjected to correlated Gaussian colored noise. Zhang and Jin [40] discussed the stationary probability density and signal-to-noise ratio of a piezoelectric energy

harvester with correlated additive and multiplicative colored noises. He et al. [41] explored the parameter resonance mechanism of nanocomposite energy harvesters based on Galerkin's method and the perturbation principle of Poincaré–Lindstedt. They found that a functionally graded reinforcement has a significant influence on the bifurcation buckling, the postbuckling path, the output voltage, and the harvested power.

Most previous results studied the energy harvesting performance of the energy harvesters subjected to stochastic external excitation by means of the stochastic averaging technique or the equivalent linearization technique. However, due to the complexity and the multistable characteristics, it is difficult to use these techniques to study multistable energy harvesters under random excitations, and there is only theoretical, numerical, and experimental investigation for multistable energy harvesters under deterministic excitations by far [27–31]. For optimal vibration energy harvesting, it is necessary and of importance to theoretically reveal the response mechanism of multistable energy harvesters subject to random parametric excitations.

The novelty of this paper is to theoretically investigate the resonance mechanism of multistable energy harvesters under narrow-band stochastic parametric excitations for improving vibration energy harvesting performance. In Section 2, the theoretical analysis framework is presented. In Section 3, based on the method of multiple scales, the largest Lyapunov exponent which determines the stability of the trivial solutions is derived. The first kind modified Bessel function is utilized to solve the theoretical solutions. In Section 4, the nontrivial solutions and their stability are provided. In Section 5, the stochastic bifurcation is analyzed for revealing the response mechanism of multistable energy harvesters by using the finite difference method. Main conclusions are addressed at last.

2. Theoretical Analysis Framework

As introduced above, several different nonlinear vibrational multistable energy harvesters were designed by far. Taking the piezoelectric pentastable energy harvester as an example to demonstrate the structure of multistable energy harvesters, the structural schematic is shown in Figure 1. The piezoelectric materials (PZTs) attached at the clamped end of the cantilever beam are used to convert vibration energy into usable electric energy, which may supply power for wireless sensors and small portable electromechanical devices. Because of the nonlinear magnetic force produced by the interaction between the tip magnet and external magnets, the pentastable energy harvester has nine equilibrium positions. **1**, **3**, **5**, **7**, and **9** are stable equilibrium positions, and intercalary **2**, **4**, **6**, and **8** are unstable equilibrium positions. Figure 2 describes the equivalent schematic diagram of the general piezoelectric multistable energy harvester which is subjected to the base excitation $x_b(t)$. In principle, the harvester may exhibit nonlinear monostable, bistable, tristable, or other multistable characteristics which mainly depend on the property of the nonlinear spring.

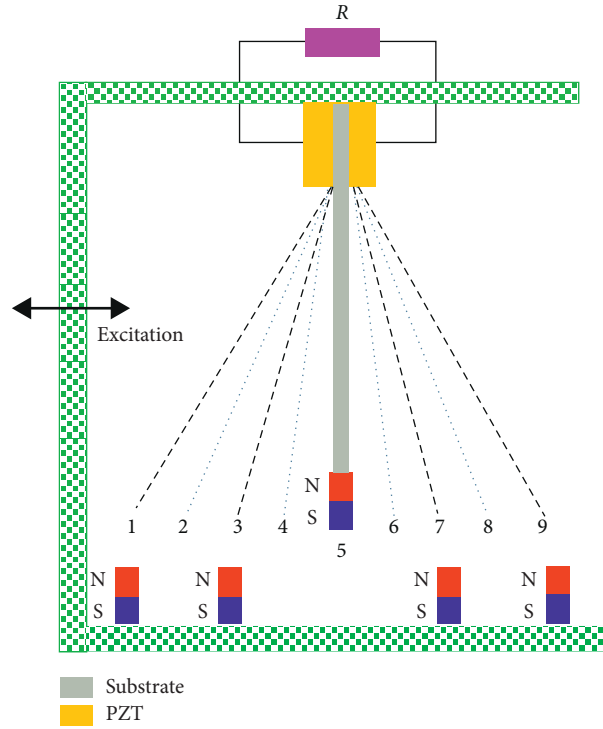


FIGURE 1: Structural diagram of the piezoelectric vibrational pentastable energy harvester.

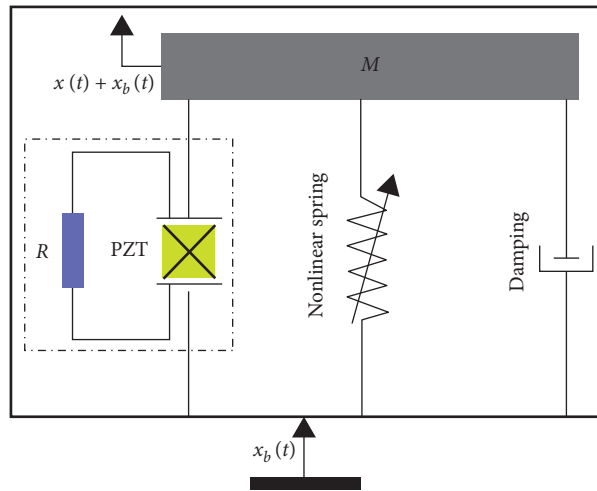


FIGURE 2: Equivalent schematic diagram of the general piezoelectric vibrational multistable energy harvester.

For the cantilever beam-based nonlinear energy harvesters, the theoretical model can be obtained based on Euler–Bernoulli beam theory, piezoelectric theory, Kirchhoff’s law, and experimental identification [17, 42]. Under the stochastic parametric excitation, the mechanical governing equation and the electrical governing equation of multistable energy harvester shown in Figures 1 and 2 can be described as follows [17, 42]:

$$M\ddot{x}(t) + C\dot{x}(t) + F_r(t) - \theta_0 v(t) = F\xi(t)x(t), \quad (1)$$

$$C_p \dot{v}(t) + v(t)(R_l)^{-1} + \theta_0 \dot{x}(t) = 0, \quad (2)$$

where $x(t)$ is the tip displacement of the harvester relative to the base. M , C , and C_p are the equivalent mass, the equivalent damping, and the equivalent capacitance, respectively. R_l and θ_0 are the load resistance and the equivalent electromechanical coupling coefficient, respectively. $v(t)$ is the output voltage. $\xi(t)$ is the stochastic excitation, and F is the density of the stochastic excitation ($F > 0$). F_r is the equivalent nonlinear restoring force (it should be noted that its opposite number $-F_r$ is the real restoring force in physics and experiments), which is the vector sum of the linear restoring force and the nonlinear

magnetic force. Its general expression can be expressed as a polynomial, as follows [17, 42]:

$$F_r = m_0 + m_1x + m_2x^2 + \dots + m_nx^n, \quad (3)$$

where $m_0, m_1, m_2, \dots, m_n$ are the polynomial coefficients. For the pentastable energy harvester, $F_r = (\omega_0^2/x_1^2x_2^2x_3^2x_4^2)x(x^2 - x_1^2)(x^2 - x_2^2)(x^2 - x_3^2)(x^2 - x_4^2)$, where ω_0 can be considered as a coefficient. It should be noted that $x=0$ is the middle stable equilibrium position of the harvester.

The stochastic excitation $\xi(t)$ is assumed as an ergodic narrow-band stochastic process with zero mean. It is governed by the following equation advanced by Wedig [43]:

$$\xi(t) = \cos(\Omega t + \hat{\gamma}W(t)), \quad (4)$$

where Ω is the center frequency, $W(t)$ is the standard Wiener process, and $\hat{\gamma}$ is the bandwidth of the stochastic excitation. The corresponding power spectrum $S_\xi(\omega)$ can be written as follows [43]:

$$S_\xi(\omega) = \frac{1}{2} \frac{\hat{\gamma}^2(\Omega^2 + \omega^2 + \hat{\gamma}^4/4)}{(\Omega^2 - \omega^2 + \hat{\gamma}^4/4)^2 + \omega^2\hat{\gamma}^4}. \quad (5)$$

Under the limiting procedure $\hat{\gamma} \rightarrow \infty$, it results in the uniformly distributed power spectrum of white noise. However, when $\hat{\gamma} \rightarrow 0$, the power spectrum $S_\xi(\omega)$ vanishes in the entire frequency range except at the singular frequency $\omega = \pm\Omega$, where $S_\xi(\omega)$ goes to infinity. The power spectrum in equation (5) is same as the power spectral density of the narrow-band filtered Gaussian white noise. In this paper, we focus on the case that $\hat{\gamma}$ is small; thus, $\xi(t)$ is bound to a narrow-band random process.

Then, for the convenience of the following analysis, the nondimensional governing equations of equations (1) and (2) are provided, as follows:

$$\ddot{x}(t) + c\dot{x}(t) + \omega^2x(t) + a_1x^3(t) + a_2x^5(t) + a_3x^7(t) + a_4x^9(t) - \theta v(t) = f\xi(t)x(t), \quad (6)$$

$$\dot{v}(t) + \lambda v(t) + g\dot{x}(t) = 0, \quad (7)$$

where $c = C/M$, $\theta = \theta_0/M$, $f = F/M$, $\lambda = 1/R_1C_p$, $g = \theta_0/C_p$, $\omega^2 = \omega_0^2/M$, $a_1 = -(\omega^2(x_1^2x_2^2x_3^2 + x_1^2x_2^2x_4^2 + x_1^2x_3^2x_4^2 + x_2^2x_3^2x_4^2)/x_1^2x_2^2x_3^2x_4^2)$, $a_2 = \omega^2(x_1^2x_2^2 + x_1^2x_3^2 + x_1^2x_4^2 + x_2^2x_3^2 + x_2^2x_4^2 + x_3^2x_4^2)/x_1^2x_2^2x_3^2x_4^2$, and $a_3 = -(\omega^2(x_1^2 + x_2^2 + x_3^2 + x_4^2)/x_1^2x_2^2x_3^2x_4^2)$; $a_4 = \omega^2/x_1^2x_2^2x_3^2x_4^2$.

The method of multiple scales [44] is applied to find the second-order analytically approximate solutions of equations (6) and (7). Firstly, the expressions of the solutions can be expressed as

$$x(t, \varepsilon) = x_0(T_0, T_1) + \varepsilon x_1(T_0, T_1) + \dots, \quad (8)$$

$$v(\tau, \varepsilon) = v_0(T_0, T_1) + \varepsilon v_1(T_0, T_1) + \dots, \quad (9)$$

where $T_n = \varepsilon^n t$ and ε is a small nondimensional bookkeeping parameter.

Denoting the differential operators by $D_0 = \partial/\partial T_0$, $D_1 = \partial/\partial T_1$, and $D_2 = \partial/\partial T_2$ and using the chain rule, the following equations can be obtained:

$$\frac{\partial}{\partial t} = D_0 + \varepsilon D_1 + \varepsilon^2 D_2 + \dots, \quad (10)$$

$$\frac{\partial^2}{\partial t^2} = D_0^2 + 2\varepsilon D_0 D_1 + \varepsilon^2(D_1^2 + 2D_0 D_2) + \dots. \quad (11)$$

To use the method of multiple scales, the system parameters could be expressed as $c = \varepsilon \hat{c}$, $a_1 = \varepsilon \hat{a}_1$, $a_2 = \varepsilon \hat{a}_2$, $a_3 = \varepsilon \hat{a}_3$, $a_4 = \varepsilon \hat{a}_4$, and $f = \varepsilon \hat{f}$. Then, substituting equations (8)–(11) into equations (6) and (7) and collecting the terms with the identical powers of ε , we have the following:

ε^0 :

$$D_0^2 x_0(T_0, T_1) + \omega^2 x_0(T_0, T_1) = 0, \quad (12)$$

$$D_0 v_0(T_0, T_1) + \lambda v_0(T_0, T_1) = -g D_0 x_0(T_0, T_1). \quad (13)$$

ε^1 :

$$\begin{aligned} D_0^2 x_1(T_0, T_1) + \omega^2 x_1(T_0, T_1) = & -2D_0 D_1 x_0(T_0, T_1) \\ & - \hat{c} D_0 x_0(T_0, T_1) \\ & - \hat{a}_1 x_0^3(T_0, T_1) \\ & - \hat{a}_2 x_0^5(T_0, T_1) \\ & - \hat{a}_3 x_0^7(T_0, T_1) \\ & - \hat{a}_4 x_0^9(T_0, T_1) \\ & + \hat{\theta} v_0(T_0, T_1) \\ & + \hat{f} \cos(\Omega T_0 + \gamma W(T_1)) \\ & \cdot x_0(T_0, T_1), \end{aligned} \quad (14)$$

where the statistical property of the standard Wiener process $\hat{\gamma}W(t) = \hat{\gamma}W(\varepsilon t)/\sqrt{\varepsilon} = \gamma W(T_1)$ is used.

According to equations (12)–(14), the first-order solutions can be written as follows:

$$x_0(T_0, T_1) = A(T_1) \cos(\omega T_0 + \varphi(T_1)), \quad (15)$$

$$\begin{aligned} v_0(T_0, T_1) = & C_0(T_1) e^{-\lambda T_0} + \frac{g\omega A(T_1)}{\lambda^2 + \omega^2} [\lambda \sin(\omega T_0 + \varphi(T_1)) \\ & - \omega \cos(\omega T_0 + \varphi(T_1))], \end{aligned} \quad (16)$$

where $A = A(T_1)$ and $\varphi = \varphi(T_1)$ are the functions of the slow time scale T_1 .

Denoting the excitation frequency as $\Omega = 2\omega + \varepsilon\sigma$ (σ is the detuning parameter), we introduce a new variable $\eta(T_1) = \sigma T_1 + \gamma W(T_1) - 2\varphi(T_1)$. Substituting equations

(15) and (16) into equation (14), the following equation can be obtained:

$$\begin{aligned}
D_0^2 x_1(T_0, T_1) + \omega^2 x_1(T_0, T_1) &= 2\omega A'(T_1) \sin(\omega T_0 + \varphi) + 2\omega A(T_1) \varphi' \cos(\omega T_0 + \varphi) + \\
&\hat{c} A(T_1) \omega \sin(\omega T_0 + \varphi) - \hat{a}_1 A^3(T_1) \cos^3(\omega T_0 + \varphi) - \hat{a}_2 A^5(T_1) \cos^5(\omega T_0 + \varphi) - \\
&\hat{a}_3 A^7(T_1) \cos^7(\omega T_0 + \varphi) - \hat{a}_4 A^9(T_1) \cos^9(\omega T_0 + \varphi) \\
&+ \hat{\theta} \left\{ C_1(T_1) e^{-\lambda T_0} + \frac{g\omega A(T_1)}{\lambda^2 + \omega^2} [\lambda \sin(\omega T_0 + \varphi) - \omega \cos(\omega T_0 + \varphi)] \right\} \\
&+ \frac{\hat{f}}{2} A(T_1) \cos \eta \cos(\omega T_0 + \varphi) - \frac{\hat{f}}{2} A(T_1) \sin \eta \sin(\omega T_0 + \varphi) \\
&+ \frac{\hat{f}}{2} A(T_1) \cos \eta \cos(3\omega T_0 + 3\varphi) - \frac{\hat{f}}{2} A(T_1) \sin \eta \sin(3\omega T_0 + 3\varphi).
\end{aligned} \tag{17}$$

Eliminating the secular terms in equation (17), we can derive

$$A'(T_1) = -\frac{\hat{\theta} g \lambda A(T_1)}{2(\lambda^2 + \omega^2)} - \frac{\hat{c}}{2} A(T_1) + \frac{\hat{f} A(T_1)}{4\omega} \sin \eta, \tag{18}$$

$$\begin{aligned}
A(T_1) \eta'(T_1) &= \sigma A(T_1) - \frac{\hat{\theta} g \omega A(T_1)}{\lambda^2 + \omega^2} - \frac{3\hat{a}_1}{4\omega} A^3(T_1) \\
&- \frac{5\hat{a}_2}{8\omega} A^5(T_1) - \frac{35\hat{a}_3}{64\omega} A^7(T_1) \\
&- \frac{63\hat{a}_4}{128\omega} A^9(T_1) + \frac{\hat{f} A(T_1)}{2\omega} \cos \eta \\
&+ \gamma A(T_1) W'(T_1).
\end{aligned} \tag{19}$$

Equations (18) and (19) are the first-order equations which govern the amplitude and the phase of the response displacement and the output voltage of the multistable energy harvester. The first-order uniform expansion of the solutions of equations (6) and (7) is given by

$$x = 2A(\varepsilon t) \cos\left(\frac{\Omega}{2}t - \frac{\eta(\varepsilon t)}{2}\right) + O(\varepsilon). \tag{20}$$

3. Trivial Solutions and Their Stability

Obviously, equations (18) and (19) have a trivial solution of $A = 0$, which corresponds to the steady-state response. Hence, the trivial steady-state solutions and their stability should be analyzed firstly. The induced linearization equations of equations (18) and (19) at the point $(0, 0)$ can be written as follows:

$$A'(T_1) = -\frac{\hat{\theta} g \lambda A}{2(\lambda^2 + \omega^2)} - \frac{\hat{c}}{2} A + \frac{\hat{f} A}{4\omega} \sin \eta, \tag{21}$$

$$A \eta'(T_1) = \sigma A - \frac{\hat{\theta} g \omega A}{\lambda^2 + \omega^2} + \frac{\hat{f} A}{2\omega} \cos \eta + \gamma A W'(T_1). \tag{22}$$

Let $\rho = \ln(A)$, and according to Itô's formula, equations (21) and (22) can be written as the following Itô stochastic differential equations:

$$d\rho = \left(-\frac{\hat{\theta} g \lambda}{2(\lambda^2 + \omega^2)} - \frac{\hat{c}}{2} + \frac{\hat{f}}{4\omega} \sin \eta \right) dT_1, \tag{23}$$

$$d\eta = \left(\sigma - \frac{\hat{\theta} g \omega}{\lambda^2 + \omega^2} + \frac{\hat{f}}{2\omega} \cos \eta \right) dT_1 + \gamma dW. \tag{24}$$

According to equations (23) and (24), the steady-state probability density $p(\eta)$ is governed by the following Fokker-Planck-Kolmogorov (FPK) equation:

$$\frac{d^2 p}{d\eta^2} - \frac{d}{d\eta} [(\bar{\sigma} - \bar{f} \cos \eta) p] = 0, \tag{25}$$

where $\bar{\sigma} = 2(\sigma - (\hat{\theta} g \omega / \lambda^2 + \omega^2)) / \gamma^2$ and $\bar{f} = -2\hat{f} / (2\omega \gamma^2)$.

Using both the periodicity condition and the normality condition [45], the solution of equations (18) and (19) can be derived, as follows:

$$p(\eta) = \frac{\exp[\bar{\sigma}(\eta + \pi) - \bar{f} \sin \eta]}{4\pi^2 I_{i\bar{\sigma}}(\bar{f}) I_{-i\bar{\sigma}}(\bar{f})} \int_{\eta}^{\eta+2\pi} [\exp(-\bar{\sigma}(y) + \bar{f} \sin y)] dy, \tag{26}$$

where $I_{i\bar{\sigma}}(\bar{f})$ and $I_{-i\bar{\sigma}}(\bar{f})$ are the first kind modified Bessel functions. η is any real or complex number. According to the multiplicative ergodic theorem [46], the Lyapunov exponent of the trivial steady-state solutions of equations (21) and (22) can be written as follows:

$$\begin{aligned}\lambda_0 &= \lim_{T_1 \rightarrow \infty} \frac{1}{T_1} \ln \left| \frac{A(T_1)}{A(0)} \right| = \lim_{T_1 \rightarrow \infty} \frac{1}{T_1} (\rho(T_1) - \rho(0)) \\ &= -\frac{\hat{\theta}g\lambda}{2(\lambda^2 + \omega^2)} - \frac{\hat{c}}{2} + \frac{\hat{f}}{4\omega} \lim_{T_1 \rightarrow \infty} \frac{1}{T_1} \int_0^{T_1} \sin \eta(\theta) d\theta \\ &= -\frac{\hat{\theta}g\lambda}{2(\lambda^2 + \omega^2)} - \frac{\hat{c}}{2} + \frac{\hat{f}}{4\omega} E[\sin \eta] = -\frac{\hat{\theta}g\lambda}{2(\lambda^2 + \omega^2)} - \frac{\hat{c}}{2} + \frac{\hat{f}}{4\omega} \\ &\quad \cdot \int_0^{2\pi} \sin \eta p(\eta) d\eta \\ &= -\frac{\hat{\theta}g\lambda}{2(\lambda^2 + \omega^2)} - \frac{\hat{c}}{2} + \frac{\hat{f}}{8\omega} \left\{ \frac{I_{1-i\bar{\sigma}}(-\bar{f})}{I_{-i\bar{\sigma}}(-\bar{f})} + \frac{I_{1+i\bar{\sigma}}(-\bar{f})}{I_{i\bar{\sigma}}(-\bar{f})} \right\},\end{aligned}\quad (27)$$

where $E[\cdot]$ denotes the mathematical expectation.

Since the response mechanism of nonlinear systems are very complex [42, 44, 47], in order to verify the aforementioned theoretical results, the parameters of equations (6) and (7) are chosen as $\hat{\theta} = 0.5$, $g = 1.0$, $\lambda = 1.0$, $\omega = 1.0$, and $\hat{c} = 0.1$. Figure 3 shows the variations of the largest Lyapunov exponent determined by equation (27). Specifically, Figure 3(a) depicts the three-dimensional plot of the largest Lyapunov exponent λ_0 . Corresponding isohypse curves of λ_0 are shown in Figure 3(b). Obviously, there exist two different ranges of the solutions for the largest Lyapunov exponents. Near the resonance area, the largest Lyapunov exponent increases to the maximum value in the center of the instability region. Outside this area, there exists a complete plane where the Lyapunov exponents are zero. To verify the results shown in Figure 3, the time-domain results in Figure 4(a) show that the trivial solution is unstable at point **A** ($\hat{f} = 1.5$ and $\sigma = 0.5$) in Figure 4(b). However, the results shown in Figure 4(b) indicate a contrary phenomenon that the trivial solution is stable at point **B** ($\hat{f} = 0.5$ and $\sigma = 0.5$).

4. Nontrivial Solutions and Their Stability

In this section, the nontrivial steady-state solutions of equations (18) and (19) will be derived. To obtain the first-order and the second-order steady-state moments of the displacement amplitude, the Itô stochastic differential equations of equations (18) and (19) can be derived, as follows:

$$dA = \left(-\frac{\hat{\theta}g\lambda A}{2(\lambda^2 + \omega^2)} - \frac{\hat{c}}{2} A + \frac{\hat{f}A}{4\omega} \sin \eta \right) dT_1, \quad (28)$$

$$\begin{aligned}d\eta &= \left(\sigma - \frac{\hat{\theta}g\omega A}{\lambda^2 + \omega^2} - \frac{3\hat{a}_1 A^2}{4} - \frac{5\hat{a}_2 A^4}{8} - \frac{35\hat{a}_3 A^6}{64} - \frac{63\hat{a}_4 A^8}{128} \right. \\ &\quad \left. + \frac{\hat{f}}{2\omega} \cos \eta \right) dT_1 + \gamma dW.\end{aligned}\quad (29)$$

For the case of $\gamma = 0$, the nontrivial steady-state solutions can be denoted as $A = A_0$ and $\eta = \eta_0$. Combining the conditions of $A' = 0$, $\eta' = 0$, and $A \neq 0$, the following relations can be derived based on equations (28) and (29):

$$-\frac{\hat{\theta}g\lambda}{2(\lambda^2 + \omega^2)} - \frac{\hat{c}}{2} + \frac{\hat{f}}{4\omega} \sin \eta_0 = 0, \quad (30)$$

$$\begin{aligned}\sigma - \frac{\hat{\theta}g\omega A_0}{\lambda^2 + \omega^2} - \frac{3\hat{a}_1 A_0^2}{4} - \frac{5\hat{a}_2 A_0^4}{8} - \frac{35\hat{a}_3 A_0^6}{64} - \frac{63\hat{a}_4 A_0^8}{128} \\ + \frac{\hat{f}}{2\omega} \cos \eta_0 = 0.\end{aligned}\quad (31)$$

When $\gamma \neq 0$, the stability of the nontrivial steady-state solutions can be examined by using the perturbation terms, as follows:

$$A = A_0 + A_1, \quad (32)$$

$$\eta = \eta_0 + \eta_1, \quad (33)$$

where A_0 and η_0 are determined by equations (30) and (31). A_1 and η_1 are the perturbation terms.

Substituting equations (32) and (33) into equations (28) and (29), neglecting the nonlinear terms, we can obtain the linearization modulation of equations (28) and (29) at A_0 and η_0 , as follows:

$$dA_1 = \frac{\hat{f}}{4\omega} A_0 \cos \eta_0 \eta_1 dT_1, \quad (34)$$

$$\begin{aligned}d\eta_1 &= \left(-\frac{3}{2} \hat{a}_1 A_0 - \frac{5}{2} \hat{a}_2 A_0^3 - \frac{105}{32} \hat{a}_3 A_0^5 - \frac{63}{16} \hat{a}_4 A_0^7 \right) A_1 dT_1 \\ &\quad - \frac{\hat{f}}{2\omega} \sin \eta_0 \eta_1 dT_1 + \gamma dW.\end{aligned}\quad (35)$$

Since equations (34) and (35) are the linear Itô stochastic differential equations, the property can be obtained by combining the moment method [48], as follows:

$$\frac{dEA_1}{dT_1} = \frac{dE\eta_1}{dT_1} = \frac{dEA_1^2}{dT_1} = \frac{dE\eta_1^2}{dT_1} = 0. \quad (36)$$

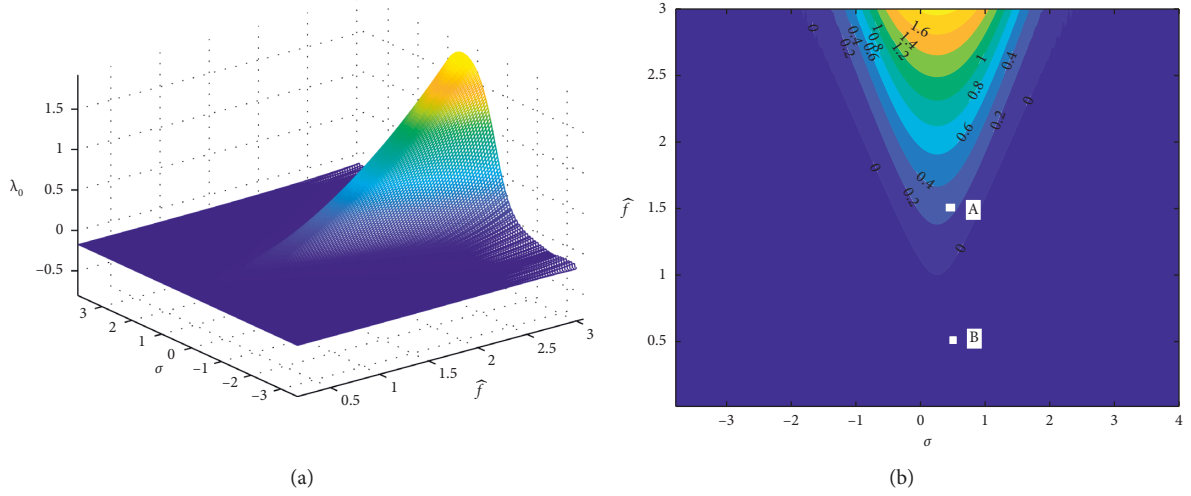


FIGURE 3: Largest Lyapunov exponents: (a) mesh surface; (b) isohypse curves.

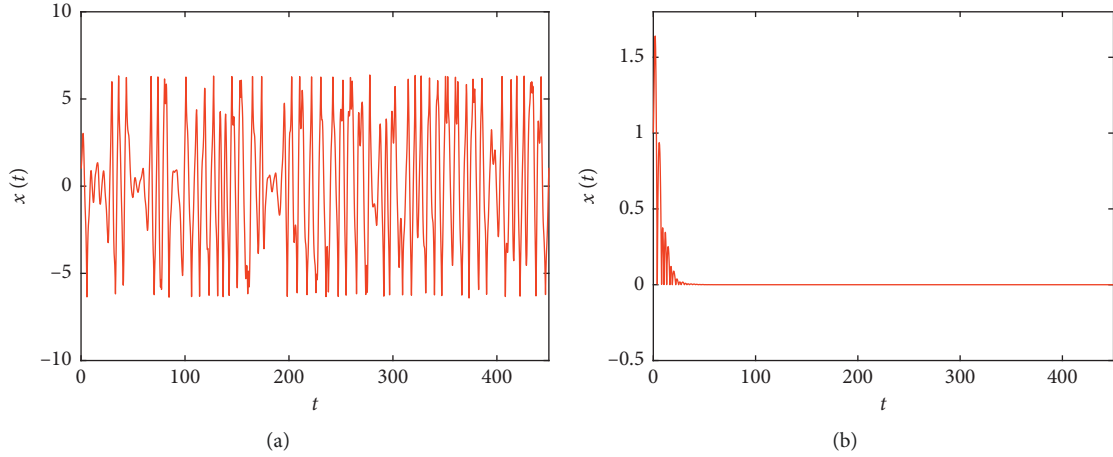


FIGURE 4: Time-domain response displacement of the multistable energy harvester: (a) $\hat{f} = 1.5$; (b) $\hat{f} = 0.5$.

The first-order and second-order steady-state moments of the nontrivial steady-state solutions of equations (34) and (35) can be derived, as follows:

$$EA_1 = E\eta_1 = 0,$$

$$EA_1\eta_1 = 0,$$

$$E\eta_1^2 = \frac{\gamma^2\omega}{\hat{f}\sin\eta_0}, \quad (37)$$

$$EA_1^2 = \frac{-\sigma + (\hat{\theta}g\omega A_0/\lambda^2 + \omega^2) + (3\hat{a}_1/4)A_0^2 + (5\hat{a}_2/8)A_0^4 + (35\hat{a}_3/64)A_0^6 + (63\hat{a}_4/128)A_0^8}{-(3/2)\hat{a}_1 - (5/2)\hat{a}_2A_0^2 - (105/32)\hat{a}_3A_0^4 - (63/16)\hat{a}_4A_0^6} \frac{E\eta_1^2}{2}.$$

Taking the expectation on both sides of equations (32) and (33), the first-order and second-order steady-state

moments of the nontrivial steady-state solutions of equations (18) and (19) can be obtained, as follows:

$$EA = E(A_0 + A_1) = A_0, \quad (38)$$

$$EA^2 = A_0^2 + EA_1^2 = A_0^2 + \frac{-\sigma + (\hat{\theta}g\omega A_0/\lambda^2 + \omega^2) + (3\hat{a}_1/4)A_0^2 + (5\hat{a}_2/8)A_0^4 + (35\hat{a}_3/64)A_0^6 + (63\hat{a}_4/128)A_0^8}{-(3/2)\hat{a}_1 - (5/2)\hat{a}_2 A_0^2 - (105/32)\hat{a}_3 A_0^4 - (63/16)\hat{a}_4 A_0^6} \cdot \frac{E\eta_1^2}{2}. \quad (39)$$

For the steady-state case, $T_0 = t \rightarrow \infty$ is satisfied, which corresponds the term $C_0(T_1)e^{-\lambda T_0}$ in equation (16) satisfied $C_0(T_1)e^{-\lambda T_0} \rightarrow 0$ with the conditions $C_0(T_1)$ bounded and $\lambda > 0$; then, the amplitude of the response voltage could be obtained:

$$V = \frac{g\omega}{\sqrt{\lambda^2 + \omega^2}} A(T_1). \quad (40)$$

The first-order and second-order steady-state moments of the voltage amplitude are

$$EV = \frac{g\omega}{\sqrt{\lambda^2 + \omega^2}} A_0, \quad (41)$$

$$EV^2 = \frac{g^2\omega^2}{\lambda^2 + \omega^2} EA^2. \quad (42)$$

For the case of $x_1 = 1.8$, $x_2 = 3.3$, $x_3 = 4.5$, and $x_4 = 5.4$, according to the expressions below equation (7), the corresponding nonlinear coefficients are $a_1 = -0.4841456090$, $a_2 = 0.06354506813$, $a_3 = -0.003049732679$, and $a_4 = 0.00004799705192$. Figures 5(a) and 5(b) indicate the first-order and second-order steady-state moments of the displacement amplitude determined by equations (38) and (39). The corresponding steady-state moments of the voltage amplitude are plotted in Figures 5(c) and 5(d). Due to the dependence on the steady-state moments of the displacement amplitude in expressions (41) and (42), the similar phenomenon could be observed in Figures 5(a)–5(d).

It can be found that the steady-state moments change along with the appearance of the multivalued response branches, which are induced by the existence of the higher-order nonlinear terms. As a comparison, another case of $a_4 = 0.0001$ (keeping other parameters being same) is also shown in Figure 5. The results showed that the response of the multistable energy harvester is very sensitive to the high-order stiffness coefficients a_4 which also have a strong influence on output voltage.

The steady-state moments of the voltage amplitude are proportional to the displacement amplitude; thus, in the following part, only the dynamic properties of the displacement amplitude are given, which also reflects the characteristics of the corresponding voltage amplitude.

For a different detuning parameter σ , the first-order steady-state moments with the variation in θ are plotted in Figure 6. The detailed response properties are presented in Table 1. When σ is small (the case of $\sigma = -1.51$ shown in Figure 6(a)), the response curve is made up of one semicircle, which is the response property I in Table 1. The larger value of σ leads to the other semicircle appearing in the region with the lower amplitude (the cases of $\sigma = -1.507$ and $\sigma = -1.5$ in Figure 6(a) and $\sigma = -1.4$ in Figure 6(b)); thus, the response curve includes two semicircles (response property II). They

combine to one continuous curve, and the critical value of σ is approximate to -1.3 (response property III). With the increase in σ , the continuous curve moves to the right side of the transverse axis (the cases of $\sigma = -1.1$ and $\sigma = -0.9$ shown in Figure 6(b); response property IV). The threshold for appearing this kind of phenomenon is $\sigma \approx -0.732$ (response property V), which means that the existence of the other two smaller semicircles could be found in the response curve. The response curve could also consist of three branches (the general case of $\sigma = -0.6$ shown in Figure 6(b); response property VI). Furthermore, the new two semicircles become larger gradually, and they finally combine to one continuous curve at $\sigma = -0.525$ (response property VII). Therefore, the response curve separates into two independent continuous curves, which can be clearly observed from the case of $\sigma = -0.3$ shown in Figure 6(c) (response property VIII).

Along with the increase in σ , it can be observed that the left continuous curve moves to the right side quickly although the continuous curve on the right side also shifts to this side. At last, they attach to each other at point **H** ($\sigma \approx -0.2666$) as response property IX shown in Table 1. Due to the further increase in σ , the curve degenerates the higher branch and the lower branch (the cases of $\sigma \approx -0.2$ shown in Figure 6(d); response property X). Increasing σ leads to the appearance of the new phenomenon, such as in the case of $\sigma \approx 0.0$ (response property XI). Then, for the larger σ , the lower branch moves to the origin point and disappears gradually, as shown in Figure 6(e) (the cases of $\sigma = 0.1$ and $\sigma = 0.3$; response property XII). Furthermore, this phenomenon is observed in the remaining branch, as shown in Figure 6(e). At the beginning, the response curve is shown by response property XIII (the case of $\sigma = 0.45$). When σ is increased to 0.4522, the independent branch degenerates to one continuous curve and one closed circle (response property XIV). It locates at the bottom of the curve, which is attached to each other at point **K**. Naturally, increasing the value of σ makes the response curve separate into two parts: the continuous curve and the closed circle (the cases of $\sigma = 0.455$ and $\sigma = 0.458$ plotted in Figure 6(e); response property XV). Due to the increase in σ , the closed circle becomes smaller and smaller. Finally, the critical case appears at $\sigma \approx 0.4582$ (response property XVI). Only one part remains as shown in Figure 6(e) for the case of $\sigma = 0.48$ (response property XVII). It can be found that the electromechanical coupling coefficient θ plays an important role in the steady-state responses of the multistable energy harvester.

The effect of the damping coefficient on the first-order steady-state moment is shown in Figure 7. It can be found that the different phenomena also appear along with the change in the damping coefficient under different detuning

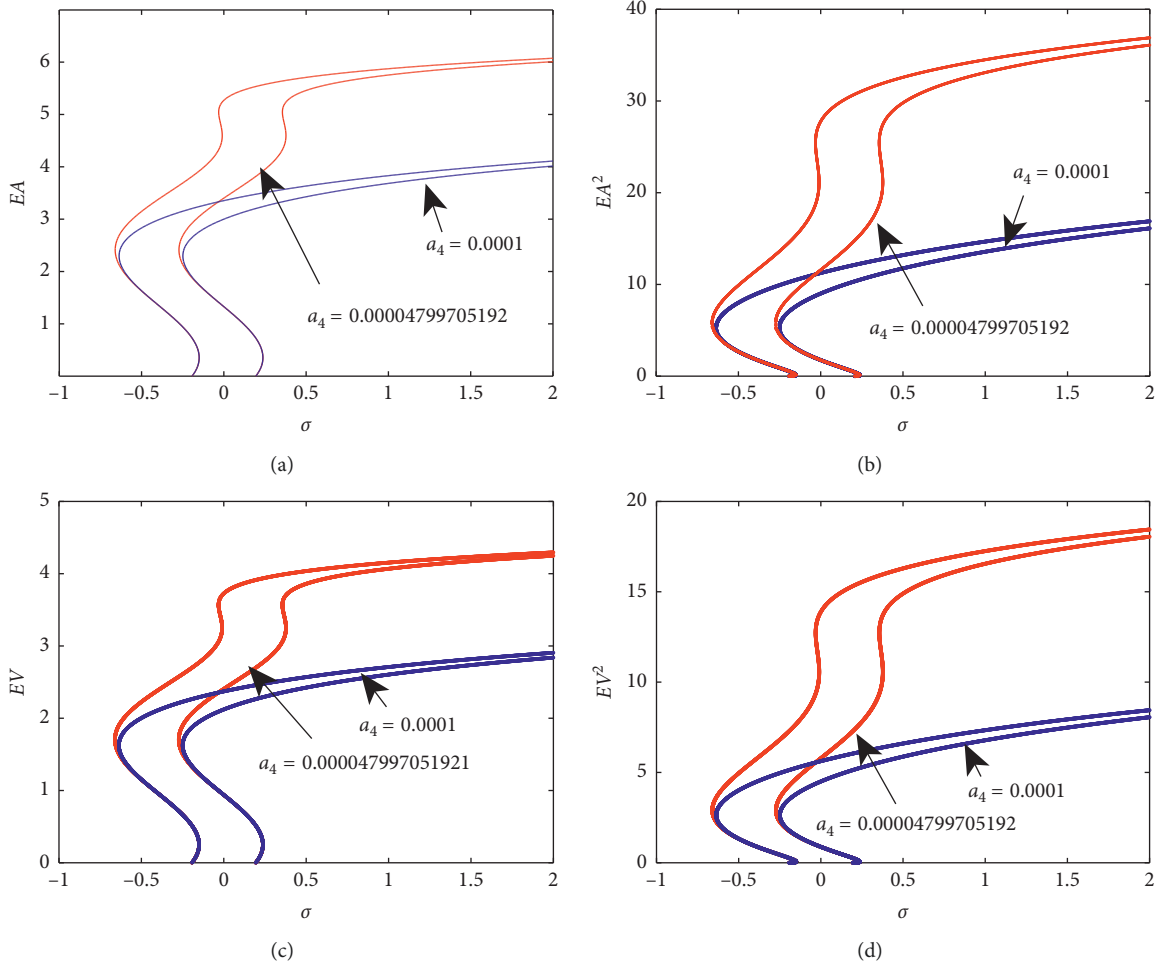


FIGURE 5: Steady-state moments of displacement and voltage of the multistable energy harvester with different high-order stiffness coefficients ($\gamma = 0.1$). (a, b) First-order and second-order steady-state moments of the displacement amplitude; (c, d) first-order and second-order steady-state moments of the voltage amplitude.

parameters. When the detuning parameter σ is small, the response curve is one independent semicircle, as shown in Figure 7(a) ($\sigma = -0.7$ and $\sigma = -0.5$). The peak point **O** at the right side turns inward, which is shown in Figure 7(a) ($\sigma = -0.35$). Furthermore, the lower branch from the original case with a single solution degenerates to the curve with two solutions for the case of $\sigma = -0.268$, which is tangent to the vertical axis at point **P**. This part shifts to the right side of the lateral axis, while the peak value in the middle of the response curve moves to the left side of the lateral axis ($\sigma = -0.2$ at point **Q**). Finally, the peak value in the middle part attaches with the vertical axis, which appears at $\sigma = -0.156$ (point **R**), as shown in Figure 7(b).

Then, the response curve separates into two parts ($\sigma = 0.1$ in Figure 7(b)). The higher branch turns inward, while the lower branch moves to the left side gradually, and the critical value can be found in Figure 7(b) for the case of $\sigma = 0.355$. Therefore, the lower branch finally disappears in Figure 7(c) for the critical case of $\sigma \approx 0.356$. For $\sigma \approx 0.473$, the remaining higher branch turns inward to the vertical axis (tangent to the vertical axis at point **S**) and the response curve degenerates into two parts. The semicircle in the lower

branch becomes smaller and smaller for the case of $\sigma = 0.495$ in Figure 7(c). Finally, only the higher branch remains for the cases of $\sigma = 0.6$, $\sigma = 0.8$, and $\sigma = 1.5$ in Figure 7(c).

As a conclusion, the damping coefficient is found to be one unavoidable factor to induce the complex dynamic properties of the multistable energy harvester.

In order to discuss the influence mechanism of stochastic noise, the bifurcation diagrams of the output voltage of the energy harvester with the variation of the excitation frequency Ω are plotted in Figure 8 under the system parameters $g = 1.0$, $\lambda = 1.0$, $\omega_0 = 1.0$, $\theta = 0.5$, $c = 0.1$, $f = 2.0$, $\sigma = 0.5$, $\gamma = 0.1$, $x_1 = 1.8$, $x_2 = 3.3$, $x_3 = 4.5$, and $x_4 = 5.4$. In Figure 8(b), the noise intensity is $\gamma = 0.1$, while the deterministic case is plotted in Figure 8(a). As can be seen that the existence of the stochastic noise has the obvious influence on the output voltage, the regular bifurcation behavior disappears; thus, the random factor could not be ignored in the energy harvesters. Two typical examples are shown in Figure 9, and the existence of the stochastic noise could induce the instability of the output voltage, which leads to the difference in the spectrum of the output voltage.

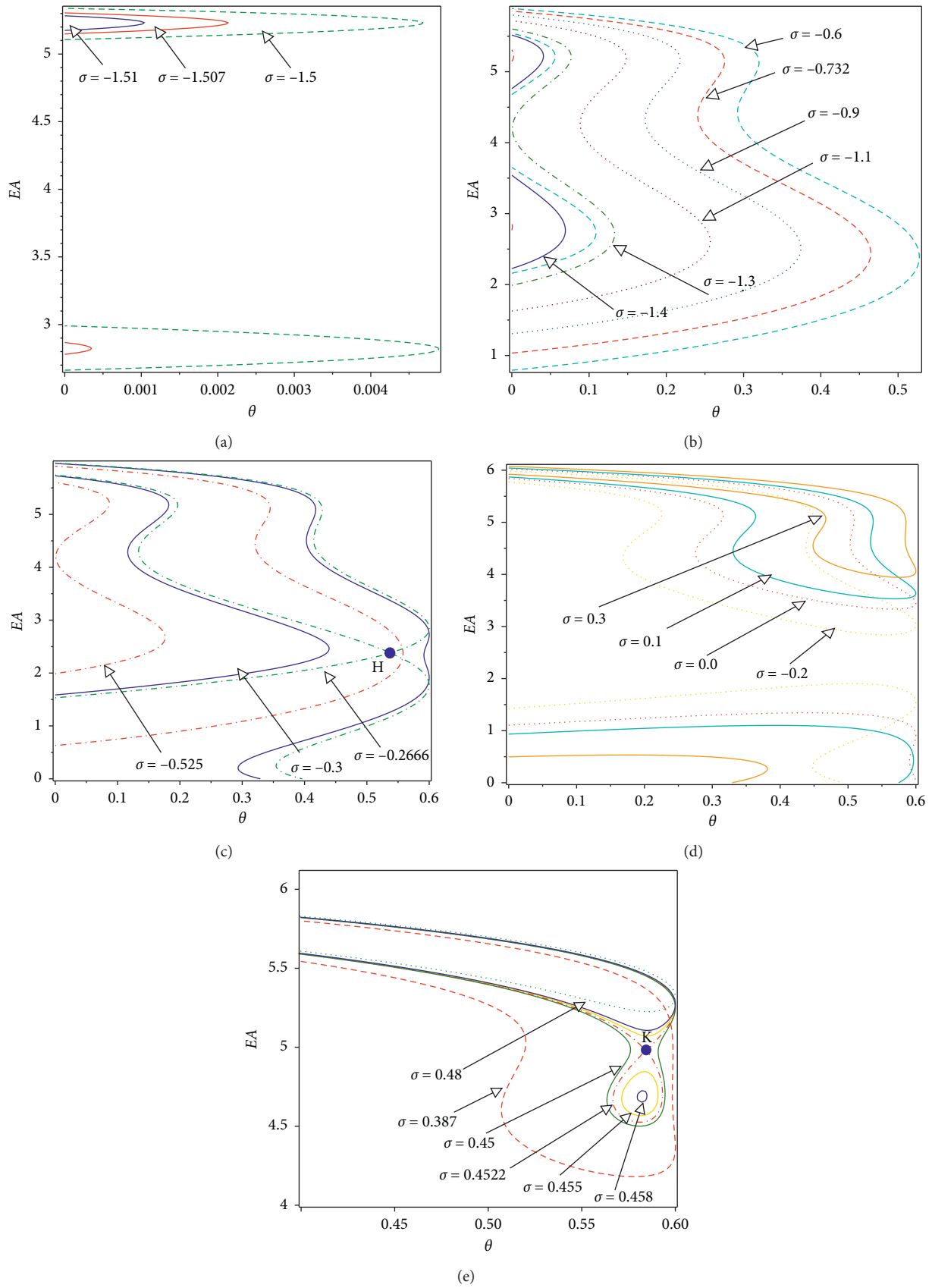


FIGURE 6: Steady-state moments of the multistable energy harvester under different detuning parameters versus θ .

TABLE 1: Response characteristics shown in Figure 6.

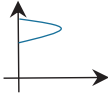
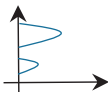
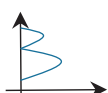




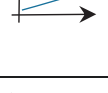
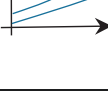
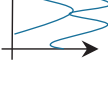
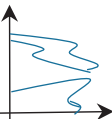
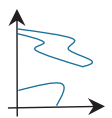
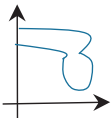
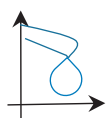
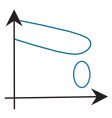
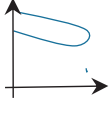
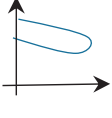
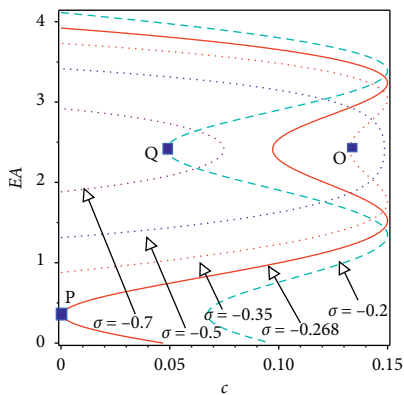
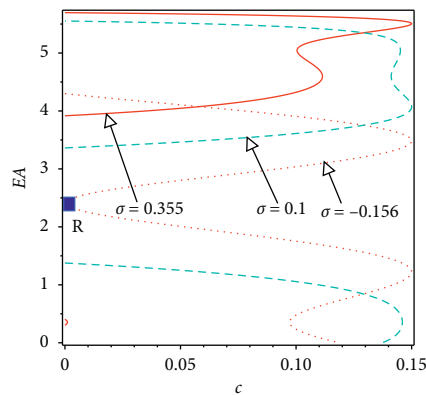
Response characteristics $\theta \rightarrow EA$		Interval range of f
I		[-1.512, -1.507]
II		[-1.507, -1.3]
III (critical case)		$\sigma \approx -1.3$
IV		(-1.3, -0.732)
V (critical case)		$\sigma \approx -0.732$
VI		(-0.732, -0.525)
VII (critical case)		$\sigma \approx -0.525$
VIII		(-0.525, -0.2666)
IX (critical case)		$\sigma \approx -0.2666$
X		(-0.2666, 0.01)

TABLE 1: Continued.

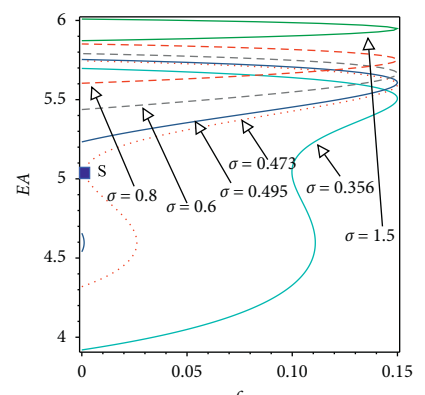
	Response characteristics $\theta \rightarrow EA$	Interval range of f
XI		[0.01, 0.063)
XII		[0.063, 0.387)
XIII		[0.387, 0.4522)
XIV (critical case)		$\sigma \approx 0.4522$
XV		(0.4522, 0.4582)
XVI		$\sigma \approx 0.4582$
XVII		(0.4582, 401)



(a)



(b)



(c)

FIGURE 7: Steady-state moments of the multistable energy harvester under different detuning parameters versus the damping coefficient.

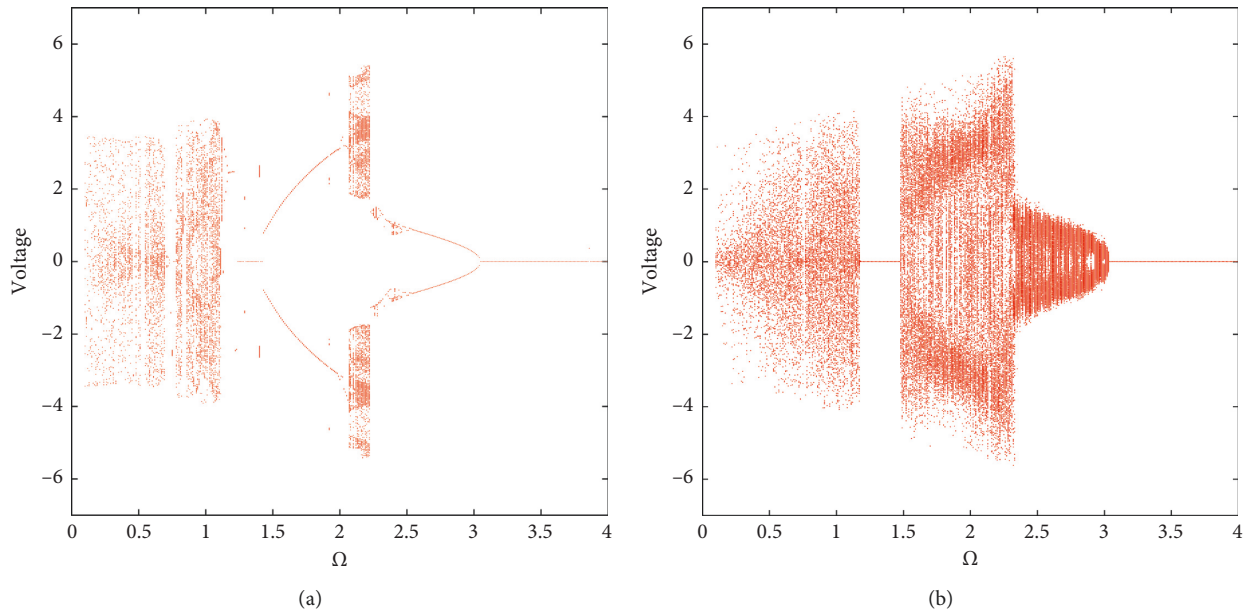


FIGURE 8: Bifurcation diagram of the output voltage with the variation in Ω : (a) $\gamma = 0.0$; (b) $\gamma = 0.1$.

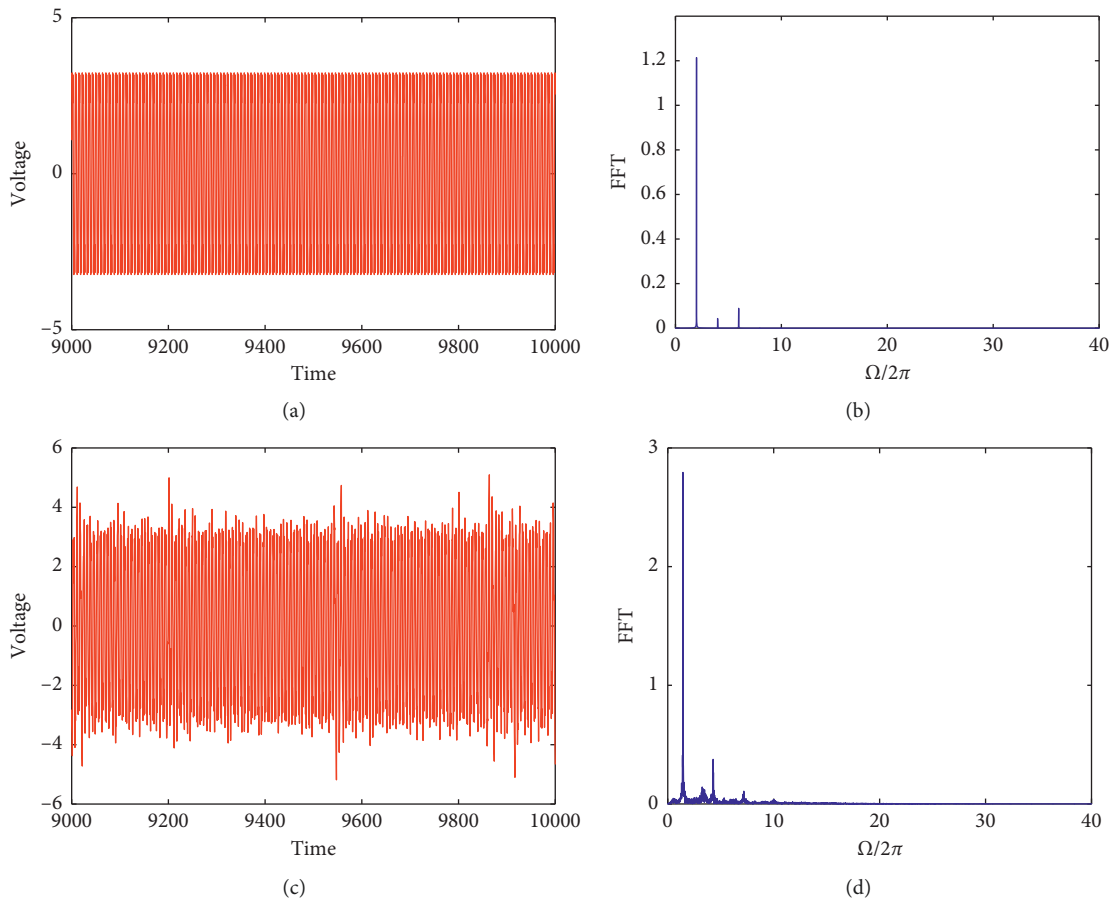


FIGURE 9: Response of the energy harvester for $\Omega = 1.8$: (a) time-domain output voltage for $\gamma = 0.0$; (b) spectrum of the time-domain output voltage for $\gamma = 0.0$; (c) time-domain output voltage for $\gamma = 0.1$; (d) spectrum of the time-domain output voltage for $\gamma = 0.1$.

Then, in Figure 10, with the variation in excitation f , the bifurcation diagram of the output voltage with $c = 0.5$, $\Omega = 3.0$, and other parameters is the same with Figure 8. The

fluctuation of the voltage is obvious in Figure 10(b), and the existence of the noise results in the change of the bifurcation characteristics of the energy harvesters. One typical example

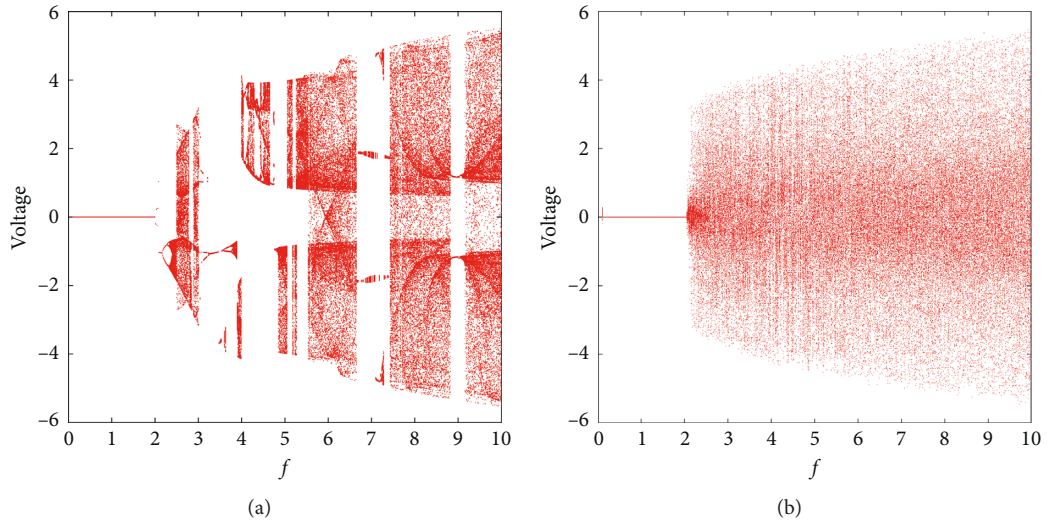


FIGURE 10: Bifurcation diagram of the output voltage with the variation in f : (a) $\gamma = 0.0$; (b) $\gamma = 0.1$.

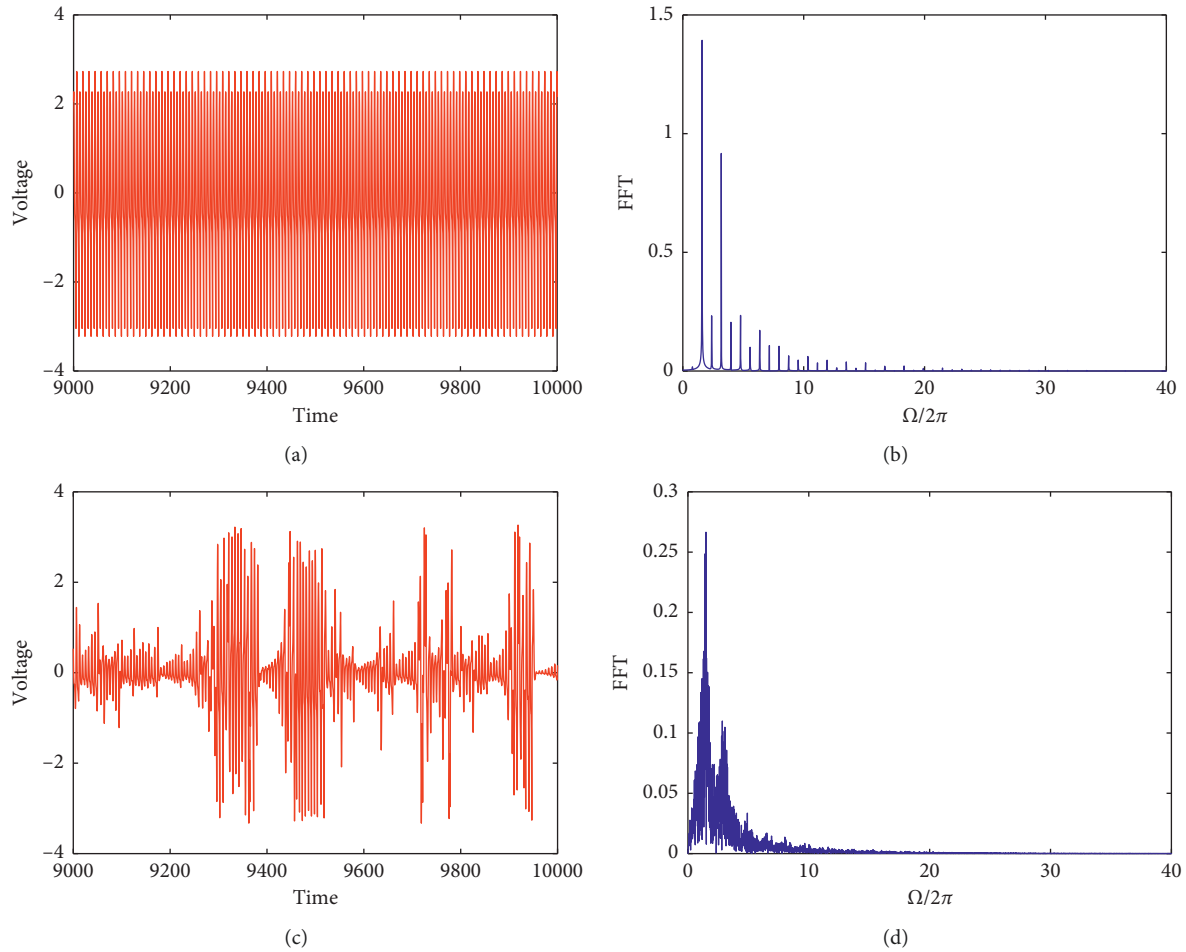


FIGURE 11: Response of the energy harvester for $f = 2.22$: (a) time-domain output voltage for $\gamma = 0.0$; (b) spectrum of the time-domain output voltage for $\gamma = 0.0$; (c) time-domain output voltage for $\gamma = 0.1$; (d) spectrum of the time-domain output voltage for $\gamma = 0.1$.

is shown in Figure 11, and it can be seen that the response curve becomes disordered in Figure 11(c), which is very different from the case without the

existence of noise. The corresponding spectrum of output voltage shown in Figures 11(b) and 11(d) also makes a big difference.

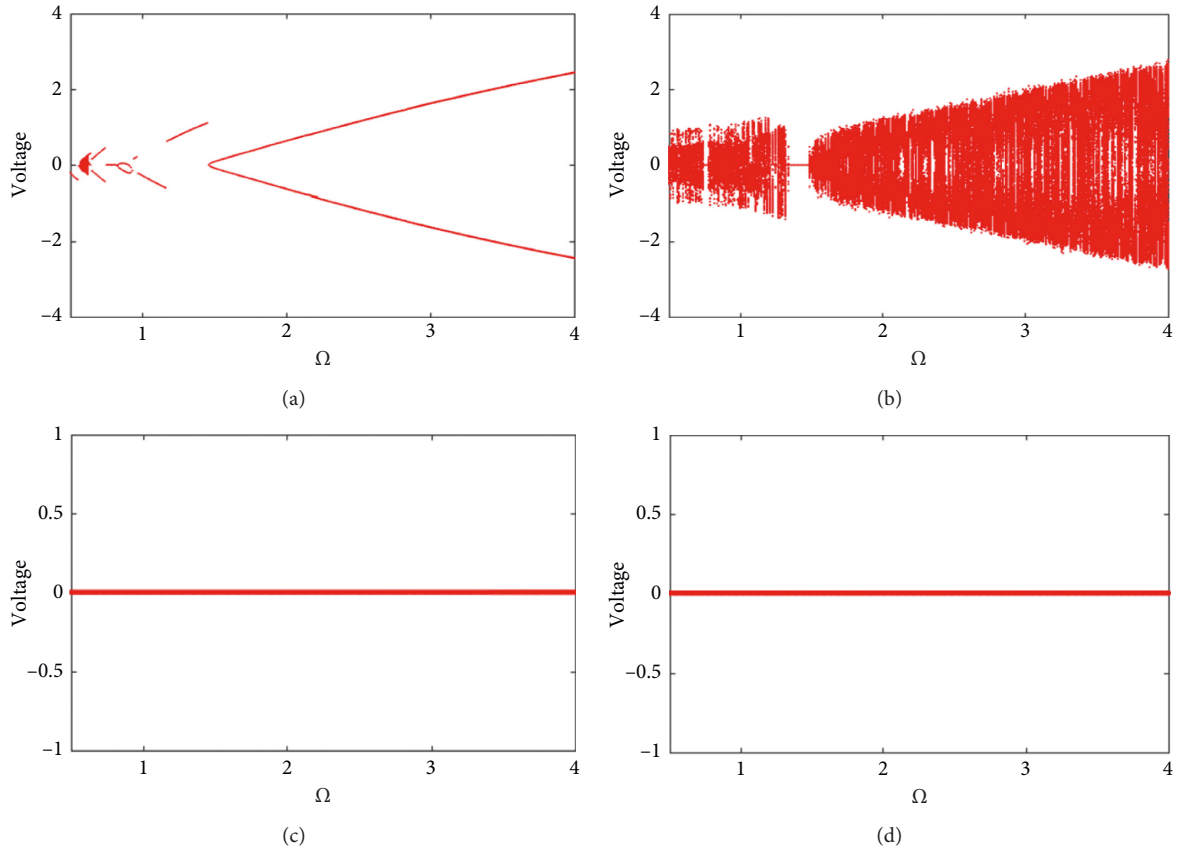


FIGURE 12: Bifurcation diagram of the output voltage with the variation in Ω : (a) $\gamma = 0.0$ for the tristable system; (b) $\gamma = 0.1$ for the tristable system; (c) $\gamma = 0.0$ for the monostable system; (d) $\gamma = 0.1$ for the monostable system.

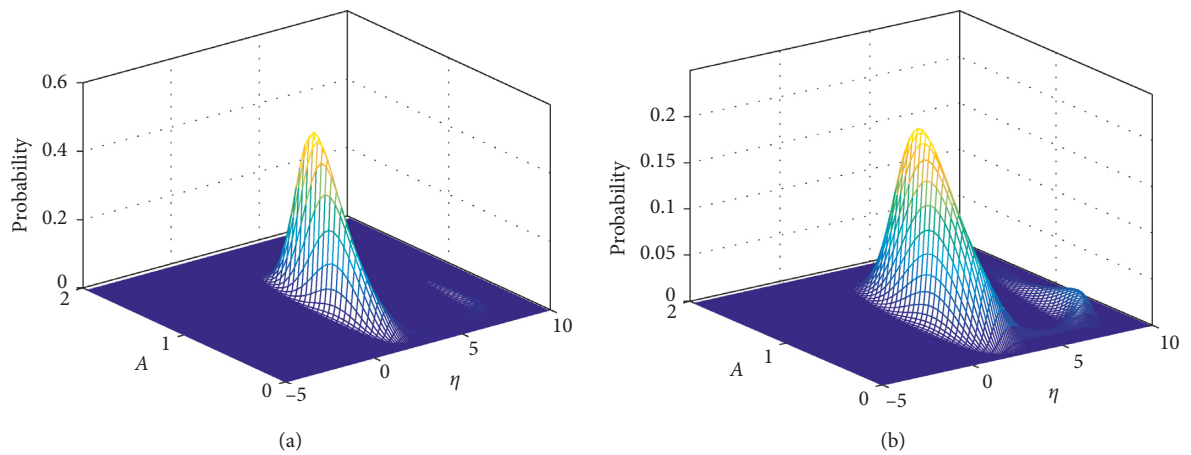


FIGURE 13: Continued.

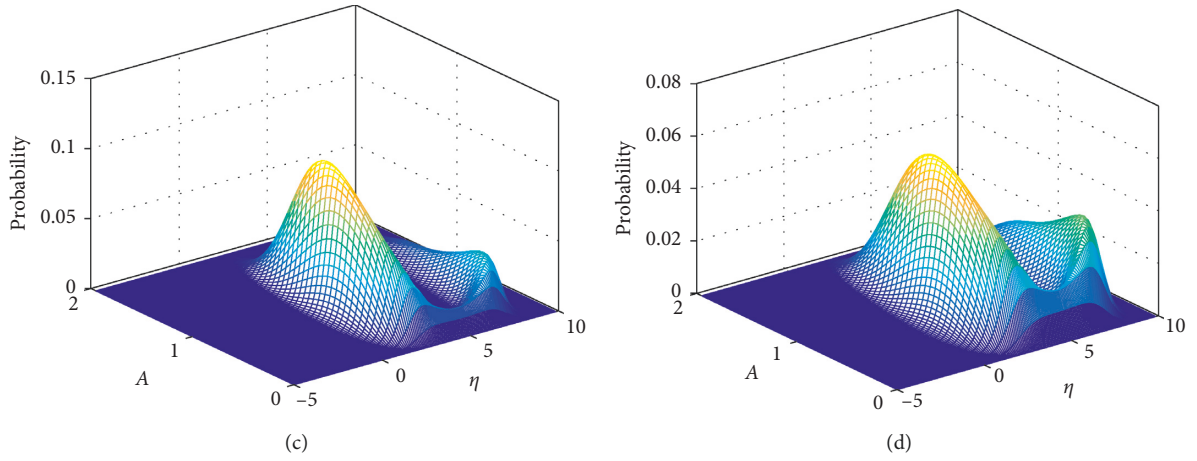


FIGURE 13: Joint probability of the multistable energy harvester: (a) $\gamma = 0.1$; (b) $\gamma = 0.2$; (c) $\gamma = 0.3$; (d) $\gamma = 0.4$.

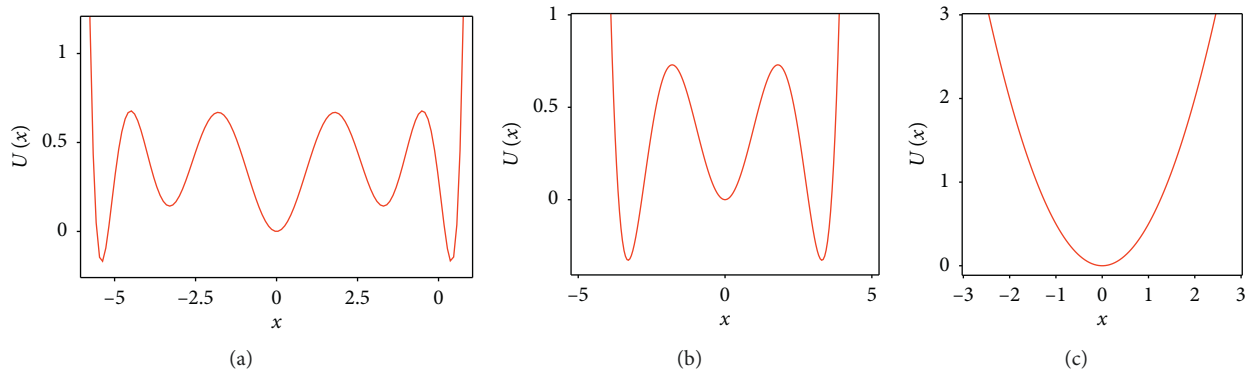


FIGURE 14: Potential energy functions: (a) pentastable energy harvester; (b) tristable energy harvester; (c) monostable energy harvester.

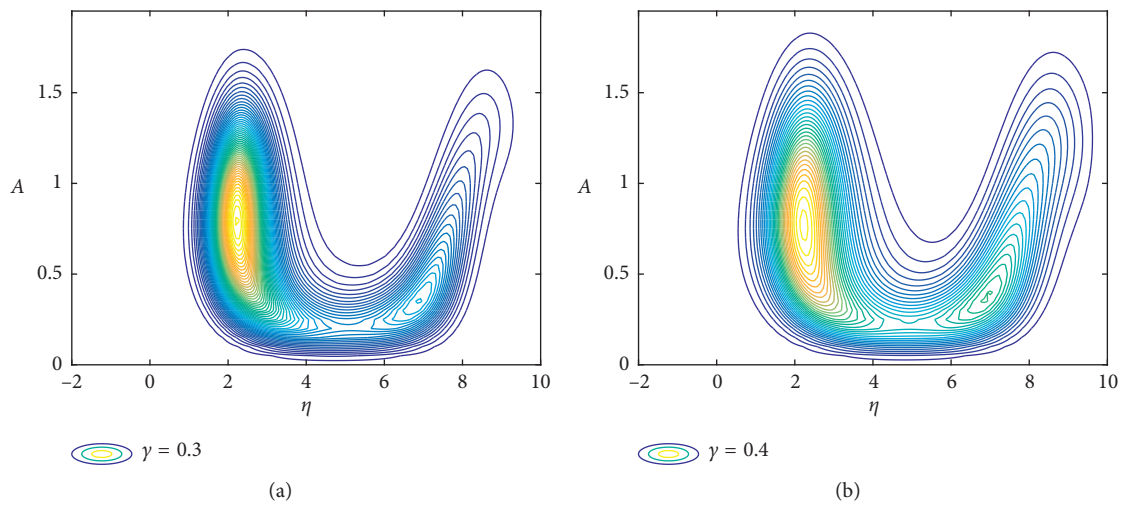


FIGURE 15: Continued.

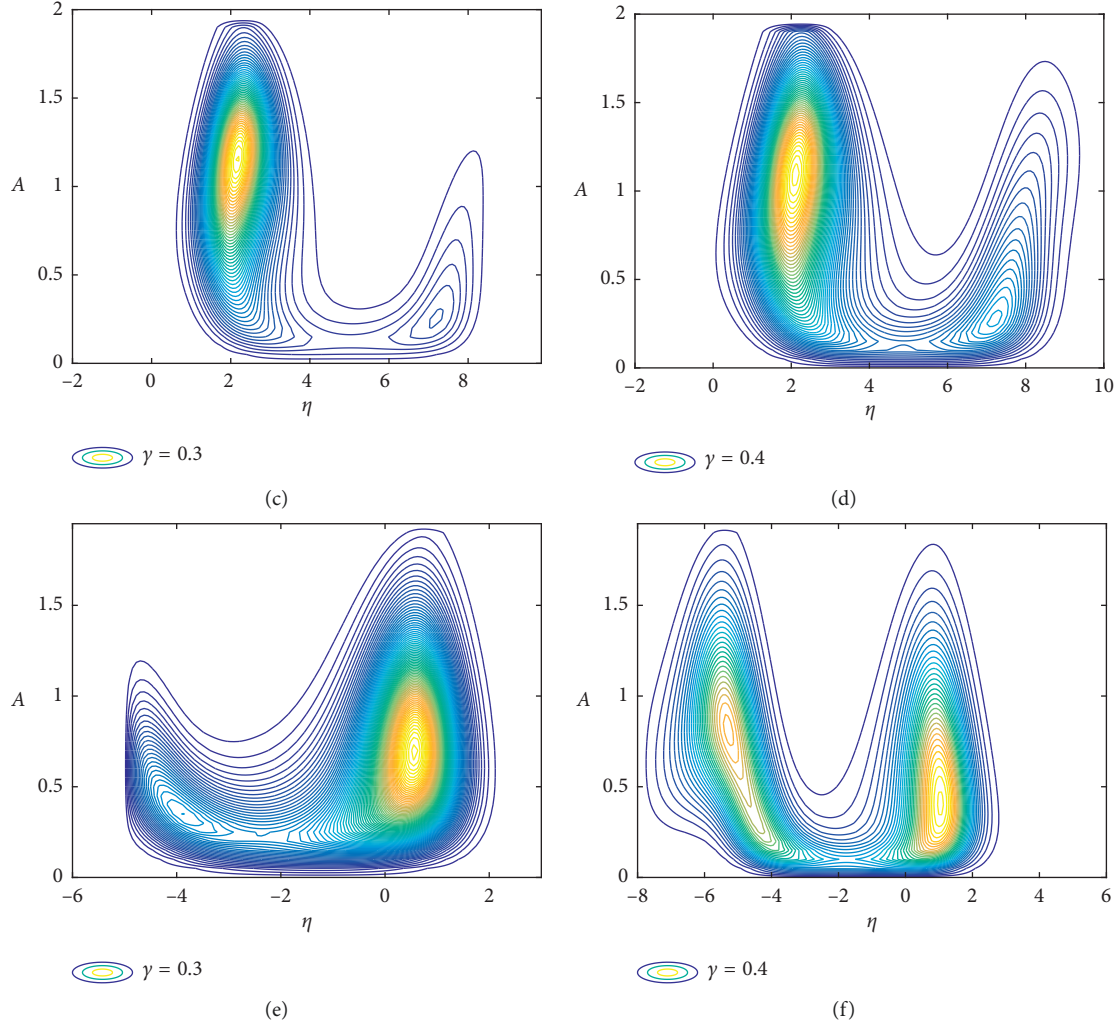


FIGURE 15: Contour surfaces: (a, b) pentastable energy harvester; (c, d) tristable energy harvester; (e, f) monostable energy harvester.

Finally, in order to consider the influence of the number of potential wells, the restoring force of the tristable and monostable energy harvesters are degraded into $F_r = (\omega_0^2/x_1^2 x_2^2)x(x^2 - x_1^2)(x^2 - x_2^2)$ and $F_r = \omega_0^2 x$, and the bifurcation diagrams of the tristable and monostable energy harvesters are shown in Figure 12, which are different from the results shown in Figure 8. The monostable energy harvesters keep the steady-state behavior; thus, the existence of noise does not lead to the fluctuation of the voltage.

5. Stochastic Bifurcation

For understanding the stochastic bifurcation phenomenon which is induced by stochastic excitations, the finite difference method [32] is used in this section. Apparently, equations (28) and (29) are two-dimensional Itô differential equations when $\gamma \neq 0$. The statistics of the responses of the multistable energy harvester can be obtained by solving the following FPK equation of equations (28) and (29):

$$\frac{\partial p}{\partial T_1} = -\frac{\partial}{\partial A} (u_1(A, \eta)p) - \frac{\partial}{\partial \eta} (u_2(A, \eta)p) + \frac{\hat{\gamma}^2}{2} \frac{\partial^2}{\partial \eta^2} (p), \quad (43)$$

where $p(A, \eta, T_1)$ is the transition probability density.

The two functions in equation (40) are defined as follows:

$$u_1(A, \eta) = -\frac{\hat{\theta}g\lambda A}{2(\lambda^2 + \omega^2)} - \frac{\hat{c}}{2}A + \frac{\hat{f}A}{4\omega} \sin \eta,$$

$$u_2(A, \eta) = \sigma - \frac{\hat{\theta}g\omega A}{\lambda^2 + \omega^2} - \frac{3\hat{a}_1}{4}A^2 - \frac{5\hat{a}_2}{8}A^4 - \frac{35\hat{a}_3}{64}A^6 - \frac{63\hat{a}_4}{128}A^8 + \frac{\hat{f}}{2\omega} \cos \eta. \quad (44)$$

The boundary condition is the natural boundary condition, while the initial distribution is assumed to be Gaussian with a probability density, as follows [49]:

$$p(A(0), \eta(0)) = \frac{1}{2\pi s_1 s_2} \exp \left\{ -\frac{(A(0) - \mu_1)^2}{2s_1^2} - \frac{(\eta(0) - \mu_2)^2}{2s_2^2} \right\}, \quad (45)$$

where $\mu_1 = (A_{\text{up}} + A_{\text{below}})/2$, $\mu_2 = (\eta_{\text{up}} + \eta_{\text{below}})/2$, $s_1 = 0.1$, and $s_2 = 0.2$.

In the following analysis, the system parameters are set as $\hat{\theta} = 0.5$, $g = 1.0$, $\lambda = 1.0$, $\omega = 1.0$, $\sigma = 0.05$, $\hat{c} = 0.1$, and $\hat{f} = 0.5$. The values of other nonlinear coefficients are same with those in Section 4. The numerical simulation is obtained in a reduced state space $[0.0, 2.0] \times [-5.0, 10.0]$. It is verified that the joint probability density can be stationary when $T \geq 15$ with the time step size of $\Delta t = 0.01$. The integral time can be defined as $T = 20$. In addition, the upwind scheme, which is accurate enough to discrete, is adopted to deal with the convective term, while the central difference scheme is applied on the diffusion term. Figure 13 shows a series of the joint probability densities of the amplitude and the phase obtained from the FPK equation solved by using the finite difference method with different bandwidths of γ .

It is found that the joint probability density concentrates at the nontrivial steady-state solution branch when $\gamma = 0.1$, as shown in Figure 13(a). The joint probability density apparently jumps downward to the trivial steady-state solution branch for $\gamma = 0.2$, as shown in Figure 13(b). Due to the increase in γ , the joint probability density continues to jump downward to the trivial steady-state solution branch for $\gamma = 0.3$ in Figure 13(c) and $\gamma = 0.4$ in Figure 13(d). The results in Figure 13 indicate that, for a lower noise intensity γ , the most probable motion of the multistable energy harvester is around the higher branch (nontrivial branch) of the amplitude response curve. However, the most probable motion of the multistable energy harvester is around the lower branch (trivial branch) of the amplitude response curve for a higher noise intensity γ . Therefore, the change in γ will induce the phenomenon of stochastic bifurcation. The direction of the jump moves from the higher branch to the lower branch along with the increase in γ .

In order to deeply investigate the probability distribution, three different energy harvesters are studied and the corresponding potential energy functions ($U(x) = \int_{-x_0}^{x_0} F_r dx$, where $-x_0$ and x_0 are the integral boundaries) are depicted in Figure 14. In detail, the equivalent nonlinear restoring forces of the tristable energy harvester and the monostable energy harvester are $F_r = (\omega_0^2/x_1^2 x_2^2)x(x^2 - x_1^2)(x^2 - x_2^2)$ and $F_r = \omega_0^2 x$, respectively. The contour surfaces for the three different energy harvesters are compared. It is found that the contour surface of the tristable energy harvester in Figures 15(c) and 15(d) is very similar to that of the pentastable energy harvester in Figures 15(a) and 15(b). For the monostable energy harvester, u_2 degenerates into $u_2(A, \eta) = \sigma - (\hat{\theta}g\omega A/\lambda^2 + \omega^2) + (\hat{f}/2\omega)\cos \eta$, as shown in Figures 15(e) and 15(f). Its response characteristic is very different with the other two harvesters. In other words, the number of stable equilibrium positions leads to variation in the distribution of the trivial and nontrivial steady-state solutions. Therefore, the appearance of the stochastic

bifurcation can be partly determined by the number of stable equilibrium points. This conclusion can be referred for the optimization design of energy harvesters for different external excitation conditions.

6. Conclusions

This paper theoretically investigates the resonance mechanism of nonlinear vibrational multistable energy harvesters under narrow-band stochastic parametric excitation. The largest Lyapunov exponent of the trivial steady-state solutions of multistable energy harvesters is deduced to analyze its stability, and the first-order and second-order steady-state moments of the nontrivial steady-state solutions are derived. It is found that the electromechanical coupling coefficient and damping coefficient greatly influence the dynamic characteristic of the steady-state moments. The stochastic bifurcation phenomenon between the nontrivial trivial steady-state solutions is revealed based on the FPK equation corresponding to the two-dimensional Itô stochastic differential equations. According to the numerical simulation results, the stationary joint probability density concentrates at the nontrivial steady-state solution branch when the intensity of the stochastic excitation is small. The probability of the trivial steady-state solution becomes larger along with the increase in the intensity of the stochastic excitation. In addition, the number of stable equilibrium points is found to influence the distribution of the trivial and nontrivial steady-state solutions. This influences the appearance of the stochastic bifurcation phenomenon and further influences the energy harvesting performance. Overall, the resonance mechanism of multistable energy harvesters under narrow-band stochastic parametric excitations has been revealed. In the future, the research framework in this paper can be referred for the optimization design of nonlinear vibrational multistable energy harvesters for different external excitation conditions.

Data Availability

All data were obtained from the methods and the equations used in this paper. Therefore, any person can obtain the data and repeat the study once the paper is published.

Conflicts of Interest

The authors declare that there are no conflicts of interest concerning the publication of this article.

Acknowledgments

This work was supported by the National Natural Science Foundation of China (Grant nos. 11702201 and 11802237), the China Postdoctoral Science Foundation (Grant no. 2018M641012), the Fundamental Research Funds for the

Central Universities (Grant no. G2018KY0306), and the 111 Project (no. BP0719007).

References

- [1] S. P. Beeby, M. J. Tudor, and N. M. White, "Energy harvesting vibration sources for microsystems applications," *Measurement Science and Technology*, vol. 17, no. 12, pp. R175–R195, 2006.
- [2] Y. Liu, X. Yang, W. Chen, and D. Xu, "A bonded-type piezoelectric actuator using the first and second bending vibration modes," *IEEE Transactions on Industrial Electronics*, vol. 63, no. 3, pp. 1676–1683, 2016.
- [3] D. Huang, R. Li, S. Zhou et al., "Theoretical analysis of vibration energy harvesters with nonlinear damping and nonlinear stiffness," *Eur Phys J Plus*, vol. 133, no. 12, p. 510, 2018.
- [4] M. Rafiee, X. Q. He, and K. M. Liew, "Non-linear dynamic stability of piezoelectric functionally graded carbon nanotube-reinforced composite plates with initial geometric imperfection," *International Journal of Non-linear Mechanics*, vol. 59, pp. 37–51, 2014.
- [5] G. Hu, J. Wang, Z. Su, G. Li, H. Peng, and K. C. S. Kwok, "Performance evaluation of twin piezoelectric wind energy harvesters under mutual interference," *Applied Physics Letters*, vol. 115, no. 7, Article ID 073901, 2019.
- [6] M. F. Daqaq, "On intentional introduction of stiffness nonlinearities for energy harvesting under white Gaussian excitations," *Nonlinear Dynamics*, vol. 69, no. 3, pp. 1063–1079, 2012.
- [7] S. Zhou, J. Cao, A. Erturk, and J. Lin, "Enhanced broadband piezoelectric energy harvesting using rotatable magnets," *Applied Physics Letters*, vol. 102, no. 17, p. 173901, 2013.
- [8] D. Huang, R. Li, and G. Yang, "On the dynamic response regimes of a viscoelastic isolation system integrated with a nonlinear energy sink," *Communications in Nonlinear Science and Numerical Simulation*, vol. 79, p. 104916, 2019.
- [9] X. Mei, S. Zhou, Z. Yang et al., "The benefits of an asymmetric tri-stable energy harvester in low-frequency rotational motion," *Applied Physics Express*, vol. 12, no. 5, Article ID 057002, 2019.
- [10] Z. H. Lai, J. L. Wang, C. L. Zhang, G. Q. Zhang, and D. Yurchenko, "Harvest wind energy from a vibro-impact DEG embedded into a bluff body," *Energy Conversion and Management*, vol. 199, Article ID 111993, 2019.
- [11] S. Fang, X. Fu, and W. H. Liao, "A music-box-like extended rotational plucking energy harvester with multiple piezoelectric cantilevers," *Applied Physics Letters*, vol. 114, no. 23, Article ID 233902, 2019.
- [12] F. Cottone, H. Vocca, and L. Gammaitoni, "Nonlinear energy harvesting," *Physical Review Letters*, vol. 102, no. 8, Article ID 080601, 2009.
- [13] G. Litak, M. I. Friswell, and S. Adhikari, "Magnetopiezoelectric energy harvesting driven by random excitations," *Applied Physics Letters*, vol. 96, no. 21, Article ID 214103, 2010.
- [14] G. Litak, M. Borowiec, M. I. Friswell, and S. Adhikari, "Energy harvesting in a magnetopiezoelectric system driven by random excitations with uniform and Gaussian distributions," *Journal of Theoretical and Applied Mechanics*, vol. 49, no. 3, pp. 757–764, 2011.
- [15] L. Chen and W. Jiang, "Internal resonance energy harvesting," *Journal of Applied Mechanics*, vol. 82, no. 3, Article ID 031004, 2015.
- [16] W. Wang, J. Cao, C. R. Bowen, D. J. Inman, and J. Lin, "Performance enhancement of nonlinear asymmetric bistable energy harvesting from harmonic, random and human motion excitations," *Applied Physics Letters*, vol. 112, no. 21, Article ID 213903, 2018.
- [17] S. Zhou, J. Cao, D. J. Inman, J. Lin, S. Liu, and Z. Wang, "Broadband tristable energy harvester: modeling and experiment verification," *Applied Energy*, vol. 133, pp. 33–39, 2014.
- [18] R. Tchoukuegno and P. Wofo, "Dynamics and active control of motion of a particle in a $\phi 6$ potential with a parametric forcing," *Physica D: Nonlinear Phenomena*, vol. 167, no. 1–2, pp. 86–100, 2002.
- [19] P. Kim and J. Seok, "Dynamic and energetic characteristics of a tri-stable magnetopiezoelectric energy harvester," *Mechanism and Machine Theory*, vol. 94, pp. 41–63, 2015.
- [20] H. Li, W. Qin, C. Lan, W. Deng, and Z. Zhou, "Dynamics and coherence resonance of tri-stable energy harvesting system," *Smart Materials and Structures*, vol. 25, no. 1, Article ID 015001, 2016.
- [21] Y. Leng, D. Tan, J. Liu, Y. Zhang, and S. Fan, "Magnetic force analysis and performance of a tri-stable piezoelectric energy harvester under random excitation," *Journal of Sound and Vibration*, vol. 406, pp. 146–160, 2017.
- [22] P. Xu, Y. Jin, and Y. Zhang, "Stochastic resonance in an underdamped triple-well potential system," *Applied Mathematics and Computation*, vol. 346, pp. 352–362, 2019.
- [23] G. T. O. Tékam, C. A. K. Kwuimy, and P. Wofo, "Analysis of tristable energy harvesting system having fractional order viscoelastic material," *Chaos: An Interdisciplinary Journal of Nonlinear Science*, vol. 25, no. 1, Article ID 013112, 2015.
- [24] S. Zhou and L. Zuo, "Nonlinear dynamic analysis of asymmetric tristable energy harvesters for enhanced energy harvesting," *Communications in Nonlinear Science and Numerical Simulation*, vol. 61, pp. 271–284, 2018.
- [25] M. Panyam and M. F. Daqaq, "Characterizing the effective bandwidth of tri-stable energy harvesters," *Journal of Sound and Vibration*, vol. 386, pp. 336–358, 2017.
- [26] D. Huang, S. Zhou, and G. Litak, "Analytical analysis of the vibrational tristable energy harvester with a RL resonant circuit," *Nonlinear Dynamics*, vol. 97, no. 1, pp. 663–677, 2019.
- [27] Z. Zhou, W. Qin, and P. Zhu, "A broadband quad-stable energy harvester and its advantages over bi-stable harvester: simulation and experiment verification," *Mechanical Systems and Signal Processing*, vol. 84, pp. 158–168, 2017.
- [28] Z. Zhou, W. Qin, Y. Yang, and P. Zhu, "Improving efficiency of energy harvesting by a novel penta-stable configuration," *Sensors and Actuators A: Physical*, vol. 265, pp. 297–305, 2017.
- [29] D. Younesian and M.-R. Alam, "Multi-stable mechanisms for high-efficiency and broadband ocean wave energy harvesting," *Applied Energy*, vol. 197, pp. 292–302, 2017.
- [30] M. Gao, Y. Wang, Y. Wang, and P. Wang, "Experimental investigation of non-linear multi-stable electromagnetic-induction energy harvesting mechanism by magnetic levitation oscillation," *Applied Energy*, vol. 220, pp. 856–875, 2018.
- [31] D. Huang, S. Zhou, and G. Litak, "Theoretical analysis of multi-stable energy harvesters with high-order stiffness terms," *Communications in Nonlinear Science and Numerical Simulation*, vol. 69, pp. 270–286, 2019.
- [32] Z. L. Huang and W. Q. Zhu, "Stochastic averaging of quasi-integrable Hamiltonian systems under bounded noise excitations," *Probabilistic Engineering Mechanics*, vol. 19, no. 3, pp. 219–228, 2004.
- [33] M. Rafiee, S. Mareishi, and M. Mohammadi, "An investigation on primary resonance phenomena of elastic medium based single walled carbon nanotubes," *Mechanics Research Communications*, vol. 44, pp. 51–56, 2012.

- [34] M. Xu, X. Jin, Y. Wang, and Z. Huang, "Stochastic averaging for nonlinear vibration energy harvesting system," *Nonlinear Dynamics*, vol. 78, no. 2, pp. 1451–1459, 2014.
- [35] M. Xu and X. Li, "Stochastic averaging for bistable vibration energy harvesting system," *International Journal of Mechanical Sciences*, vol. 141, pp. 206–212, 2018.
- [36] W.-A. Jiang and L.-Q. Chen, "Stochastic averaging of energy harvesting systems," *International Journal of Non-Linear Mechanics*, vol. 85, pp. 174–187, 2016.
- [37] W.-A. Jiang and L.-Q. Chen, "An equivalent linearization technique for nonlinear piezoelectric energy harvesters under Gaussian white noise," *Communications in Nonlinear Science and Numerical Simulation*, vol. 19, no. 8, pp. 2897–2904, 2014.
- [38] Q. He and M. F. Daqaq, "New insights into utilizing bistability for energy harvesting under white noise," *Journal of Vibration and Acoustics*, vol. 137, no. 2, Article ID 021009, 2015.
- [39] D. Liu, Y. Xu, and J. Li, "Probabilistic response analysis of nonlinear vibration energy harvesting system driven by Gaussian colored noise," *Chaos, Solitons & Fractals*, vol. 104, pp. 806–812, 2017.
- [40] Y. Zhang and Y. Jin, "Stochastic dynamics of a piezoelectric energy harvester with correlated colored noises from rotational environment," *Nonlinear Dynamics*, vol. 98, no. 1, pp. 501–515, 2019.
- [41] X. Q. He, M. Rafiee, and S. Mareishi, "Nonlinear dynamics of piezoelectric nanocomposite energy harvesters under parametric resonance," *Nonlinear Dynamics*, vol. 79, no. 3, pp. 1863–1880, 2014.
- [42] A. Erturk and D. J. Inman, *Piezoelectric Energy Harvesting*, Wiley, Chichester, UK, 2011.
- [43] W. V. Wedig, "Invariant measures and Lyapunov exponents for generalized parameter fluctuations," *Structural Safety*, vol. 8, no. 1–4, pp. 13–25, 1990.
- [44] A. H. Nayfeh and D. T. Mook, *Nonlinear Oscillations*, Wiley, Chichester, UK, 2008.
- [45] H. Rong, G. Meng, X. Wang, W. Xu, and T. Fang, "Invariant measures and Lyapunov exponents for stochastic mathieu system," *Nonlinear Dynamics*, vol. 30, no. 4, pp. 313–321, 2002.
- [46] Y. I. Oseledec, "A multiplicative ergodic theorem: Lyapunov characteristic number for dynamical systems," *Trans Moscow Math Society*, vol. 19, pp. 197–231, 1968.
- [47] J. H. Yang, M. A. F. Sanjuán, H. G. Liu, G. Litak, and X. Li, "Stochastic P-bifurcation and stochastic resonance in a noisy bistable fractional-order system," *Communications in Nonlinear Science and Numerical Simulation*, vol. 41, pp. 104–117, 2016.
- [48] Y. Lin and G. Cai, *Probabilistic Structural Dynamics: Advanced Theory and Applications*, McGraw-Hill, New York, NY, USA, 2004.
- [49] J. S. Yu and Y. K. Lin, "Numerical path integration of a non-homogeneous Markov process," *International Journal of Non-Linear Mechanics*, vol. 39, no. 9, pp. 1493–1500, 2004.

